Solitonic excitations in the Ising anisotropic chain BaCo2 V2O8 under large transverse magnetic field

Quentin Faure, Shintaro Takayoshi, Béatrice Grenier, Sylvain Petit, Stéphane Raymond, Martin Boehm, Pascal Lejay, Thierry Giamarchi, V. Simonet

Solitonic excitations in the Ising anisotropic chain $BaCo_2V_2O_8$ under large transverse magnetic field

Quentin Faure,[1,2,3] Shintaro Takayoshi,[4,*] Béatrice Grenier,[1] Sylvain Petit,[5,†] Stéphane Raymond,[1] Martin Boehm,[6] Pascal Lejay,[2] Thierry Giamarchi,[7] and Virginie Simonet[2]

[1]*Université Grenoble Alpes, CEA, IRIG/MEM/MDN, F-38000 Grenoble, France*
[2]*Université Grenoble Alpes, CNRS, Institut Néel, 38000 Grenoble, France*
[3]*London Centre for Nanotechnology and Department of Physics and Astronomy, University College London, London WC1E 6BT, United Kingdom*
[4]*Department of Physics, Konan University, Kobe 658-8501, Japan*
[5]*Laboratoire Léon Brillouin, CEA, CNRS, Université Paris-Saclay, CE-Saclay, F-91191 Gif-sur-Yvette, France*
[6]*Institut Laue Langevin, CS 20156, F-38042 Grenoble, France*
[7]*Department of Quantum Matter Physics, University of Geneva, CH-1211 Geneva, Switzerland*

(Received 6 July 2021; revised 19 November 2021; accepted 23 November 2021; published 29 December 2021)

We study the dynamics of the quasi-one-dimensional Ising-Heisenberg antiferromagnet $BaCo_2V_2O_8$ under a transverse magnetic field. Combining inelastic neutron scattering experiments and theoretical analyses by field theories and numerical simulations, we mainly elucidate the structure of the spin excitation spectrum in the high-field phase, appearing above the quantum phase transition point $\mu_0 H_c \approx 10$ T. We find that it is characterized by collective solitonic excitations superimposed on a continuum. These solitons are strongly bound in pairs due to the effective staggered field induced by the nondiagonal g tensor of the compound and are topologically different from the fractionalized spinons in the weak-field region. The dynamical susceptibility numerically calculated with the infinite time-evolving block decimation method shows an excellent agreement with the measured spectra, which enables us to identify the dispersion branches with elementary excitations. The lowest-energy dispersion has an incommensurate nature and has a local minimum at an irrational wave number due to the applied transverse field.

DOI: 10.1103/PhysRevResearch.3.043227

I. INTRODUCTION

Intensive efforts are currently being made to investigate materials exhibiting prominent quantum effects. In this context, magnetic systems of low dimensionality make undeniable contributions with a host of different phases exhibiting strong quantum effects such as Bose-Einstein condensation [1,2] spin solids and spin liquid phases [3,4] with exotic excitations [5,6].

In the simplest case of a spin-1/2 Heisenberg chain with antiferromagnetic interactions, the ground state is strongly entangled, lacks long-range order, and hosts fractionalized excitations called spinons [7]. Those peculiar excitations, quite different from classical spin waves, possess a topological nature, can be understood as domain walls that disrupt the Néel order, and can be observed as a continuum in inelastic neutron scattering measurements. Such physics has been realized and probed in many different experimental realizations ranging from chains to ladders, e.g., in the quantum Heisenberg spin chains $KCuF_3$ and $CuSO_4 \bullet 5D_2O$ [8,9] or the quantum spin ladder $(C_5H_{12}N)_2CuBr_4$ [10].

Systems with relatively small exchange constants provide a new avenue to study this physics, since applying a magnetic field becomes an efficient control parameter, very similar in spirit to a voltage gate for itinerant systems [11], changing the position and even the nature of the excitation and pushing the system through quantum phase transitions. In anisotropic one-dimensional (1D) magnets, for instance, applying a uniform magnetic field along the Ising axis closes the gap to the lowest excitations in a way consistent with a Pokrovsky-Talapov transition [12] and leads to an incommensurate phase [13–15] with Tomonaga-Luttinger liquid (TLL) spin dynamics [16–18]. For a field perpendicular to the Ising axis, one-dimensional magnetic systems undergo a quantum phase transition belonging to the well-known Ising universality class [19]. Few experimental realizations of the one-dimensional Ising model in a transverse field have been realized so far, e.g., in the ferromagnetic spin-chain compound $CoNb_2O_6$ [20,21] or more recently in the antiferromagnetic spin chains $BaCo_2V_2O_8$ [22–24] and $SrCo_2V_2O_8$ [25–27].

Among the very rich class of materials realizing quasi-one-dimensional physics, $BaCo_2V_2O_8$ (see Fig. 1) has indeed proven to be a specially fascinating example. In this material, Co^{2+} ions form screw chains along the **c** axis and carry *effective* spins 1/2 coupled by antiferromagnetic exchange. Several ingredients make it even richer: (i) The chains possess a significant Ising anisotropy in the **c** "chain" direction, which

*Corresponding author: takayoshi@konan-u.ac.jp
†Corresponding author: sylvain.petit@cea.fr

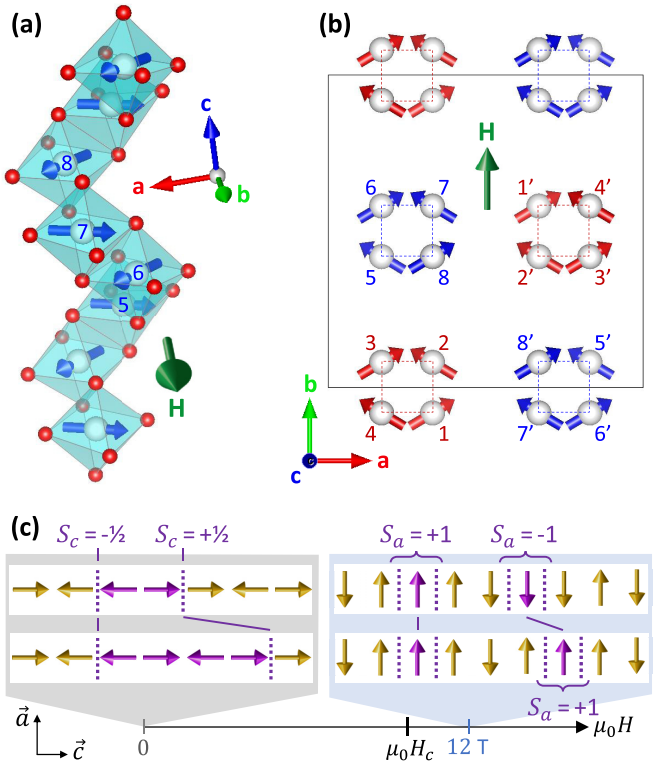

FIG. 1. Canted antiferromagnetic structure of the Co^{2+} screw chains of $BaCo_2V_2O_8$ in a 12 T transverse magnetic field applied along the **b** axis (shown by the dark green arrow): (a) perspective view of one chain (the Co and O atoms are white and red, respectively; the CoO_6 octahedra are materialized in light blue; and the Co^{2+} spins are represented by the blue arrows); (b) projection in the (**a**, **b**) plane of the two types of Co chains, with red (blue) spins for the chains having a 4_1 (4_3) screw axis symmetry. Two chains of the same type correspond to each other by the lattice centering $\frac{1}{2}(\mathbf{a}+\mathbf{b}+\mathbf{c})$. In both (a) and (b), the labeling of the Co atoms is the same as in Refs. [15,23]. At 12 T, the 0.92-μ_B antiferromagnetic component of the magnetic moment is aligned along the **a** axis with a field-induced 0.55-μ_B ferromagnetic component along the **b** direction. (c) Phase diagram as a function of the applied transverse magnetic field with a sketch of the soliton excitations and their time evolution on both sides of the critical field. At zero field, the spinon excitations carry a spin $S_c = \pm 1/2$, corresponding to the topological index of the excitation, and hop by two sites along the chain axis when time evolves. At 12 T in the high-field phase, the elementary excitations carry a topological index $S_a = \pm 1$, hop by one site when time evolves, and are dual from the low-field spinons [23].

is modeled by an anisotropic exchange tensor with still sizable components in the **a** and **b** directions; (ii) the g tensor has off-diagonal staggered parts, which allows one to effectively apply a staggered magnetic field to the system when applying experimentally a uniform magnetic field [28]; (iii) the interchain dispersion is non-negligible and quite complex due to the screw nature of the chains. As a result, $BaCo_2V_2O_8$ has been a perfect laboratory to tackle the exotic physics of low-dimensional quantum magnets.

Without a magnetic field, $BaCo_2V_2O_8$ shows a long-range Néel order below $T_N = 5.5$ K where the spins align antiferromagnetically along the **c** axis, i.e., the direction of Ising anisotropy [29]. In the presence of such Néel order the spinons, which would be free for an isolated single chain, are confined by the linear potential due to the interchain coupling, giving rise to a series of bound states, which have been observed by neutrons [30] as a series of discrete excitations, in agreement with theoretical expectations. Similar effects have been reported in the sister compound studied in Refs. [31,32]. Note that although existing for a 3D compound, those modes, also called Zeeman ladders [33], are different from classical spin waves, a remarkable result which is due to the small yet sizable value of the interchain coupling. It is worth noting that, in the case of an antiferromagnetic spin chain, any staggered field, arising from interchain couplings as described above or from nondiagonal terms in the g tensor, was shown both experimentally [23,30,34,35] and analytically [36–38] to confine spinons.

The staggered parts in the g tensor are responsible for an even richer situation. The system undergoes a transition at $\mu_0 H_c \approx 10$ T that was identified [22,23,39], by a combination of field theory, numerical analysis, and neutron scattering experiments, as a spin-flop transition from the **c** to **a** direction. This transition, which is in the same universality class as the celebrated transverse field Ising model one [19], is characterized by different topological excitations above and below $\mu_0 H_c$ [23] and is generally described by a dual-field double sine-Gordon model [40]. The evolution of the spin correlations as measured by polarized neutrons was studied for fields up to 12 T with a special focus on the low-energy modes, including their nature and polarization.

The aim of this paper is to continue such investigations in the high-field phase, above the transition, combining an inelastic neutron scattering study of the spin-spin correlations with a theoretical analysis based on the model that was introduced in Ref. [23]. Such an analysis is particularly useful in the case of $BaCo_2V_2O_8$ given its complexity and the various ingredients at play, namely, the spin anisotropy, the interchain coupling, and the "two" magnetic fields (uniform and staggered) effectively applied to the system due to the nature of the g tensor. The comparison between measurements and theory allows us to precisely analyze the spectrum of the new soliton excitations in the high-field phase and to thoroughly disentangle the influence of the various ingredients at play in $BaCo_2V_2O_8$ on the physics of this phase. This is especially important for the two components of the magnetic field since the uniform one is responsible for the incommensurability of the spin excitations while the staggered one is the one determining the quantum phase transition. Although most of the properties are well in line with the model introduced in Ref. [23], some yet unexplained additional features emerge, such as a tetramerization of the spectrum.

The plan of the paper is as follows: Sec. II provides the details of our experimental and theoretical approaches. Section III describes the neutron measurements of the spin-spin correlation functions and their interpretation in terms of the corresponding numerical simulations, based essentially on the infinite time-evolving block decimation (iTEBD) technique [41] with a mean-field treatment of the coupling between the chains. We focus in particular on the identification of the collective modes and on their polarization. Section IV discusses these results in the light of a simplified model

introduced to better understand and highlight the important features of the dispersions. Conclusions and perspectives are found in Sec. V.

II. SYSTEM, MODEL, AND METHODS

In this section, we describe how to model the target material, $BaCo_2V_2O_8$, as a quasi-one-dimensional spin system, schematically represented in Fig. 1. We also explain our experimental and theoretical methods to study the microscopic mechanisms at the origin of the dynamics of the system.

A. Experimental measurements

The $BaCo_2V_2O_8$ single crystal was grown at Institut Néel by the floating-zone method [42]. It was aligned with the **b**-axis vertical yielding $(\mathbf{a}^\star, \mathbf{c}^\star)$ as the horizontal scattering plane and placed in a cryomagnet providing a maximum uniform field of 12 T at a base temperature of 1.5 K. Inelastic neutron scattering (INS) experiments were performed on two cold-neutron triple-axis spectrometers, Three-Axis instrument for Low Energy Spectroscopy (ThALES) and Forschungszentrum Jülich Collaborating Research Group (FZJ-CRG) IN12, both installed at Institut Laue Langevin (ILL, France). On ThALES [43], a PG(002) monochromator (analyzer) was used to select (analyze) the initial (final) wave vector of the unpolarized neutron beam. On IN12, the spin of the incident neutrons was polarized using a cavity transmission polarizer located far upstream in the guide. The initial wave vector was selected by a PG(002) monochromator, and both the final wave vector and neutron polarization were analyzed using a Heusler analyzer (see Ref. [44] for a more detailed description of the standard polarized neutron setup on IN12). On both spectrometers, the energy resolution was of the order of 0.15 meV, and the high-order harmonics were suppressed by a velocity selector. The polarization analysis performed on IN12 uses the classical (X, Y, Z) frame where the X axis is aligned with the scattered wave vector $\mathbf{Q}$, the Z axis is vertical, and the Y axis is perpendicular to $\mathbf{Q}$ and Z. The strong applied vertical magnetic field (up to 12 T) restricts the polarization analysis to the so-called P_Z channel. Scattering which involves a spin flip then encodes the correlations between Y components of the spins, while the non-spin-flip scattering encodes the correlations between Z components (on top of the nuclear scattering). Importantly, the vertical current of the Mezei spin flipper, placed just before the monochromator on IN12, was calibrated for every used value of the incident wave vector and of the magnetic field. The horizontal current was checked to be nonsensitive to the applied field. The flipping ratios were determined using a graphite sample: Their values ranged between 12 and 23, depending on the incident wave vector and magnetic field values.

B. Model

We consider the model Hamiltonian for $BaCo_2V_2O_8$

$$\mathcal{H} = J\sum_{n,\mu}\left[\epsilon\left(S^a_{n,\mu}S^a_{n+1,\mu} + S^b_{n,\mu}S^b_{n+1,\mu}\right) + S^c_{n,\mu}S^c_{n+1,\mu}\right] - \sum_{n,\mu}\mu_0\mu_B\mathbf{H}\cdot\tilde{g}\mathbf{S}_{n,\mu} + J'\sum_{n}\sum_{\langle\nu\mu\rangle}S^c_{n,\mu}S^c_{n,\nu}, \quad (1)$$

also used in Ref. [23]. The first term is the XXZ Hamiltonian where $\mathbf{S}_{n,\mu}$ is a spin-1/2 operator, μ is the chain index, n is the site index, $J = 5.8$ meV is the antiferromagnetic (AFM) intrachain exchange coupling, and $\epsilon = 0.53$ is the magnetic anisotropy. The second term is the Zeeman term arising from the application of the magnetic field. μ_B is the Bohr magneton, $\tilde{g}$ is the Landé g tensor, and $\mathbf{H}$ is the external magnetic field (applied along the **b** axis). The last term describes the weak interchain coupling. We consider here the simplest form for this coupling, namely, a uniform antiferromagnetic unfrustrated nearest-neighbor term. Note that the precise nature of the interchain coupling in $BaCo_2V_2O_8$ is still largely unknown with most likely more complex terms occurring due to the screw nature of the chains [45]. The interchain term taken here should thus be seen as a phenomenological term, resulting potentially from the average of several individual couplings. The value giving at zero magnetic field the best comparison with the experimental results for the spinon confinement [23] is $J' = 0.17$ meV. This is the value that we take in this paper.

Due to tilting of the ligands of Co^{2+}, the $\tilde{g}$ tensor becomes nondiagonal [28]. The influence of an applied uniform field along the **b** axis given this $\tilde{g}$ tensor is then described by

$$\mathbf{H}\cdot\tilde{g}\mathbf{S}_{n,\mu} = H\left[g_{ba}(-1)^n S^a_{n,\mu} + g_{bb}S^b_{n,\mu} + g_{bc}\cos\left(\pi\frac{2n-1}{4}\right)S^c_{n,\mu}\right], \quad (2)$$

with $g_{ba}/g_{bb} = 0.40$, $g_{bc}/g_{bb} = 0.14$, and $g_{bb} = 2.35$. The third term in Eq. (2) is a four-site periodic field, but its effect is negligible [23].

Owing to the effective staggered field [first term in Eq. (2)] induced by the nondiagonal $\tilde{g}$ tensor, it is favorable for the spins to cant from the **c** to **a** direction with increasing applied field. A quantum phase transition eventually occurs at around $\mu_0 H_c \approx 10$ T, above which the spins are essentially aligned along the **a** axis and get progressively polarized by the uniform field in the **b** direction [see Figs. 1(a) and 1(b)]. Moreover, this transition can be considered as a topological transition as it separates two phases which host different types of topological excitations. The latter are dual from each other and well described by the double-sine Gordon model [23]. Below $\mu_0 H_c$, the excitations are spinons, while they become solitons carrying a topological index $S_{x(=a)} = \pm 1$ along the **a** direction above $\mu_0 H_c$. In Ref. [23], the evolution of the spectrum under a transverse magnetic field up to 12 T was studied. Special attention was paid to the lowest-energy excitations at selected positions of the reciprocal space, but the instructive full spectrum of the solitons in the high-field phase was not investigated. In the subsequent sections of this paper we focus on this point and investigate by inelastic neutron scattering the dispersion along the **c** axis of the solitonic excitations above the critical field H_c.

C. Numerical calculations

In the theoretical approach employed in this paper, we treat the interchain coupling in Eq. (1) using a mean-field approximation

$$J'\sum_{n}\sum_{\langle\mu,\nu\rangle}S^c_{n,\mu}S^c_{n,\nu} \simeq J'\sum_{n,\mu}\sum_{\langle\nu\rangle_\mu}S^c_{n,\mu}\langle S^c_{n,\nu}\rangle,$$

which allows us to reduce the quasi-1D problem to an effective one-dimensional one in the presence of a (self-consistent) staggered field. Mean fields arising from interchain coupling with S^a and S^b are much smaller than the magnetic field and are thus considered as negligible. Therefore the Hamiltonian is recast into the simple chain problem

$$\mathcal{H} = J\sum_n \left[\epsilon\left(S^a_n S^a_{n+1} + S^b_n S^b_{n+1}\right) + S^c_n S^c_{n+1}\right] - \mu_0\mu_B H \times \sum_n \left[g_{ba}(-1)^n S^a_n + g_{bb} S^b_n + g_{bc}\cos\left(\pi\frac{2n-1}{4}\right)S^c_n\right] + \tilde{h}_c\sum_n (-1)^n S^c_n, \quad (3)$$

where $\tilde{h}_c = J'|\langle S^c_n\rangle|$ is an effective staggered field induced by the interchain coupling. Note that the number of nearest-neighbor chain sites is only due to the spiral structure of Co^{2+} ions.

For the numerical simulations, we first obtain the ground state of the Hamiltonian using the infinite density matrix renormalization group (iDMRG) [46] and then calculate the retarded spin-spin correlation function,

$$C_{\alpha\beta}(\mathbf{r}, t) = -i\theta_s(t)\langle\left[S^\alpha_{\mathbf{r}}(t), S^\beta_0(0)\right]\rangle$$

[$\theta_s(t)$ is the step function], by using iTEBD [41] with infinite boundary conditions [47]. The dynamical susceptibility is the Fourier transform of the retarded correlation function,

$$\chi_{\alpha\beta}(\mathbf{Q}, \omega) = \int_{-\infty}^{\infty} dt \sum_{\mathbf{r}} e^{i(\omega t - \mathbf{Q}\cdot\mathbf{r})} C_{\alpha\beta}(\mathbf{r}, t),$$

which is related to the INS spectrum $S(\mathbf{Q}, \omega)$ by

$$S(\mathbf{Q}, \omega) \propto \sum_{\alpha,\beta=x,y,z}\left(\delta_{\alpha,\beta} - \frac{Q_\alpha Q_\beta}{|\mathbf{Q}|^2}\right) S_{\alpha\beta}(\mathbf{Q}, \omega),$$

where $S_{\alpha\beta}(\mathbf{Q}, \omega) = |\mathrm{Im}\,\chi_{\alpha\beta}(\mathbf{Q}, \omega)|$ at low temperature. For the calculations of the INS spectrum (especially the lattice Fourier transform), we employ the actual positions of Co^{2+} ions. The dimension of the matrix product representation for iDMRG and iTEBD is 60, the discrete time step is $dt/(\epsilon J)^{-1} = 0.05$, and the spin-spin correlation is calculated for the time interval $0 \leqslant dt/(\epsilon J)^{-1} \leqslant 60$ or 80.

To better identify the excitations, we shall also consider a simplified model where the spins occupy the sites of a simple linear chain:

$$\mathcal{H} = J\sum_n \left[\epsilon\left(S^a_n S^a_{n+1} + S^b_n S^b_{n+1}\right) + S^c_n S^c_{n+1}\right] - g_{ba}\mu_B\mu_0 H\sum_n (-1)^n S^a_n - g_{bb}\mu_B\mu_0 H\sum_n S^b_n. \quad (4)$$

III. RESULTS

In this section, we present the results of the INS measurements and elucidate the dynamics of $BaCo_2V_2O_8$ under the large transverse magnetic field by comparing the experimental data with the theory essentially based on the numerical simulation.

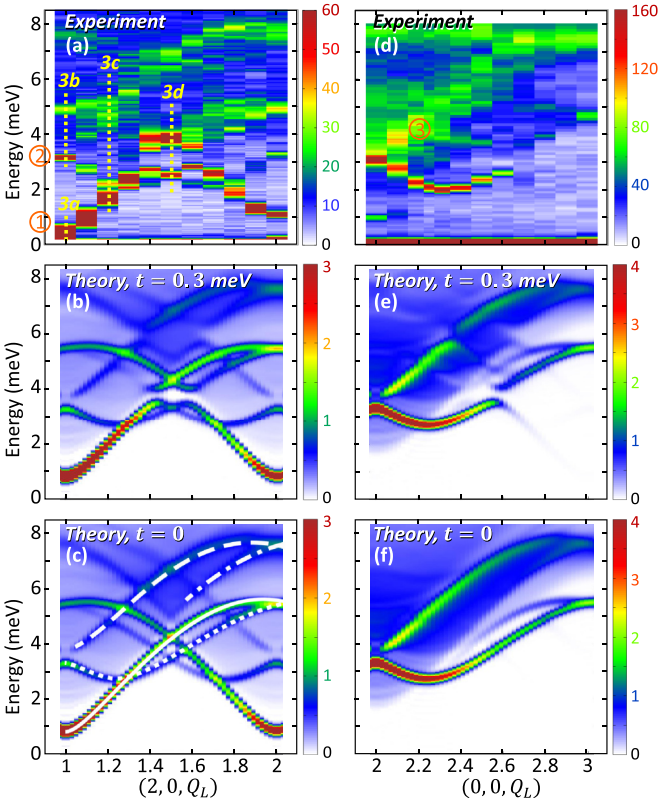

FIG. 2. Inelastic scattering intensity maps showing the intrachain dispersion of the magnetic excitations along (a)–(c) $\mathbf{Q} = (2, 0, Q_L)$ and (d)–(f) $\mathbf{Q} = (0, 0, Q_L)$, in a transverse field of 12 T applied along the **b** axis: (a) and (d) maps obtained experimentally on ThALES and IN12, respectively, from a series of constant-**Q** energy scans, compared with the numerically calculated neutron scattering cross section [48] (b) and (e) of a tetramerized chain with $t = 0.3$ meV and (c) and (f) of a uniform chain ($t = 0$), as explained in the text. In (a), the yellow dotted lines show the energy scans presented in Figs. 3(a)–3(d), and the first three modes are labeled in (a) and (b) by the orange numbers. The white lines in (c) correspond to the same three modes plus a fourth one, all sketched in Fig. 6 with the same symbols (solid, dotted, dashed, and dash-dotted lines for modes 1, 2, 3, and 4, respectively). Constant-**Q** energy scans along $(2, 0, Q_L)$ and $(0, 0, Q_L)$ comparing experimental and calculated data are shown in Appendix C.

A. Spin dynamics along the chain

The spectrum of the magnetic excitations measured by means of INS at $\mu_0 H = 12$ T is plotted in Figs. 2(a) and 2(d). The experimental intensity maps are constructed from constant-**Q** energy scans taken along $(2, 0, Q_L)$ and $(0, 0, Q_L)$. They were recorded with a 0.1-r.l.u. step in Q_L (where r.l.u. refers to reciprocal lattice units) and an energy transfer varying between 0.2 and 8.2 meV.

As already reported in Ref. [23], the discrete Zeeman ladder spectrum characterizing the zero-field spin dynamics (see Fig. 1 in Ref. [30]) becomes less evident when increasing the uniform field and is lost above the $\mu_0 H_c \approx 10$ T critical field which signals the quantum phase transition. The present results at 12 T exhibit well-defined branches, drastically different from these Zeeman ladders. Some diffuse intensity is

also observed above 2 meV, which reflects underlying continua of excitations. Note that "spurious" (parasitic) intensities were identified in the map of Fig. 2(d) at about 1 meV around $Q_L = 2$ due to a contamination from a Bragg peak and around 7.5 meV for $2 \leqslant Q_L \leqslant 2.6$ due to the Bragg scattering from the aluminum frame of the analyzer.

The low-energy excitations characterized by the largest spectral weight are labeled as modes 1 and 2 [see Fig. 2(a)]. Leaving aside the anticrossing at $\mathbf{Q} = (2, 0, 1.5)$ discussed below, mode 1 disperses throughout the Brillouin zone from 0.4 meV at $Q_L = 1$, up to 5.5 meV at $Q_L = 2$. Mode 2 is observed at 3.2 meV for $Q_L = 1$ and disperses downwards and then upwards reaching also 5.5 meV at $Q_L = 2$. The third branch, labeled as mode 3, especially visible in Fig. 2(d), starts from 3.2 meV at $Q_L = 2$ and disperses up to 7 meV at $Q_L = 3$. An extinction in the spectral weight, at ≈3 meV, is observed for various Q_L values, especially clearly around $\mathbf{Q} = (2, 0, 1.5)$ and $\mathbf{Q} = (0, 0, 2.6)$. It is attributed to an anticrossing between modes 1 and 2.

The numerically calculated INS spectra with the Hamiltonian equation (1) in a magnetic field of $\mu_0 H = 12$ T are displayed in Figs. 2(c) and 2(f). They are in good agreement with the experiment. The well-defined excitations coexist with a continuum, especially visible in the $\mathbf{Q} = (0, 0, Q_L)$ map with a minimum of ≈2 meV at $Q_L = 2$. These results, however, do not reproduce the anticrossing at the wave vector $Q_L = 1/2$. It is instructive to translate this wave vector using the reduced reciprocal units associated with the fictitious lattice spacing $c_0 = c/4$ between two neighboring Co^{2+} ions along the chain direction. The physical meaning of the anticrossing point at $\frac{2\pi}{c} Q_L = \frac{1}{2}\frac{\pi}{2c_0}$ is the loss of the four-site translational symmetry. The original band and its shifted replica by $\frac{\pi}{2c_0}$ are coupled, yielding the opening of a gap at the crossing point. Although the last term in Eq. (2), which is four-site periodic, may be a good candidate, the result of numerical calculations [Figs. 2(c) and 2(f)] shows that its influence is negligible and cannot be the cause of the anticrossing. To describe this anticrossing, we add a phenomenological isotropic tetramerization term

$$-t \sum_n \sum_\mu \sqrt{2} \cos\left(\pi \frac{2n+1}{4}\right) \mathbf{S}_{n,\mu} \cdot \mathbf{S}_{n+1,\mu} \qquad (5)$$

to the Hamiltonian equation (1). In Figs. 2(b) and 2(e), we display the calculated spectra for the tetramerization parameter $t = 0.3$ meV. This additional ingredient indeed accounts for the anticrossing, which quite remarkably is already observed at zero magnetic field [30]. The origin of this tetramerization could not be determined on experimental grounds and remains unclear at the present stage. It would require, for instance, an additional symmetry lowering with respect to the tetragonal to orthorhombic one already reported [49]. At least, our results indicate that the four-site periodic perturbation can cause the anticrossing at the proper wave vector. We discuss in more detail this anticrossing and its possible origin in Sec. IV.

B. Spin polarization of the excitations

The polarization of the various excitations in the high-field phase can be further studied both experimentally and numerically. To this end, inelastic neutron scattering experiments

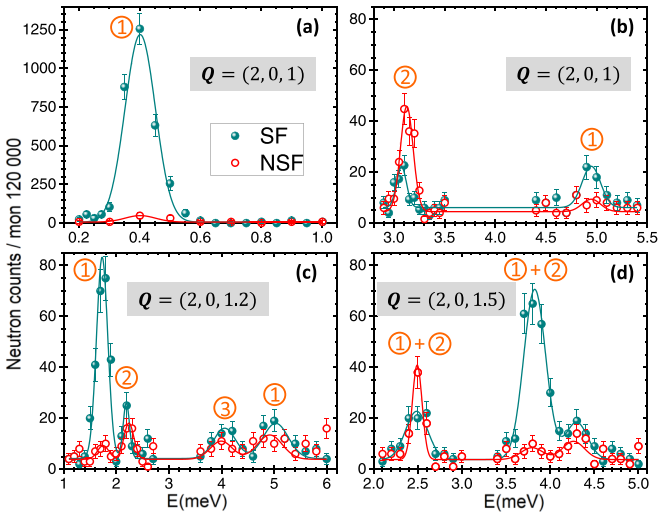

FIG. 3. Constant-**Q** energy scans measured on IN12 using polarized neutrons in the spin-flip (SF) and non-spin-flip (NSF) channels at (a) and (b) $\mathbf{Q} = (2, 0, 1)$, (c) $\mathbf{Q} = (2, 0, 1.2)$, and (d) $\mathbf{Q} = (2, 0, 1.5)$. These scans are materialized by the yellow dotted lines on the map of Fig. 2(a). Note the about 16 times larger intensity scale for (a) as compared with (b)–(d). The SF intensity corresponds to fluctuations occurring in the (**a**, **c**) plane and perpendicular to the scattering vector **Q**, while the NSF one corresponds to fluctuations along the **b** axis. Here, neutron monitor (mon).

were conducted on IN12, using polarized neutrons. Since a strong magnetic field (12 T) is applied along the vertical **b** axis, the spin flip (SF) and non-spin-flip (NSF) channels correspond to correlations between spin components perpendicular to the scattering wave vector **Q** within the (**a**, **c**) plane and between spin components along the **b** axis, respectively. Figure 3 shows constant-**Q** energy scans performed in both channels at the Q_L positions and E ranges spotted in Fig. 2(a) by the yellow dotted lines.

The SF data allow us to follow mode 1 (green points in Fig. 3). It is visible at 0.4 meV for $Q_L = 1$ and at 1.7 meV for $Q_L = 1.2$ and is distributed on both sides of the anticrossing for $Q_L = 1.5$. Hence it is mostly polarized in the (**a**, **c**) plane. We can further deduce that its polarization is along the **c** axis as it is absent in the $\mathbf{Q} = (0, 0, Q_L)$ map. Mode 1 is thus a transverse fluctuation, with respect to the ordered antiferromagnetic moments (along **a**), and involves spin components along **c**. In the same Q_L range, mode 2 appears with a larger intensity in the NSF channel (red points in Fig. 3) at $Q_L = 1$ and 3.15 meV, showing that it is more polarized along the **b** axis than in the other two directions [see Figs. 3(b)–3(d)]. It becomes more mixed with the other polarizations at higher energy. This confirms our previous understanding of these modes and definitely demonstrates their transverse character, perpendicular to the ordered moments in the high-field phase [23]. Mode 3, visible at 4 meV in Fig. 3(c), seems to present equal SF and NSF contributions, which should result from a mixture of the **a**, **b**, and **c** polarizations.

These experimental determinations of the magnetic excitation polarization have been further inspected using iTEBD calculations. Figures 4(a)–4(c) show the components of dynamical structure factors calculated at 12 T for $t = 0$

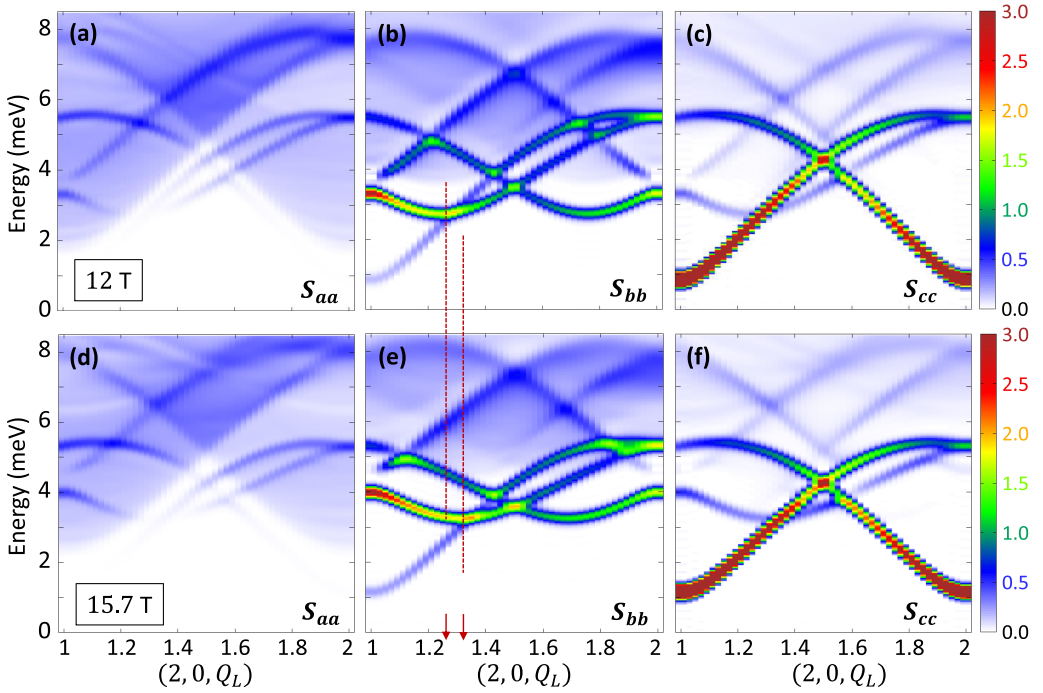

FIG. 4. (a)–(c) S_{aa}, S_{bb}, and S_{cc} components of the intensity color map calculated at 12 T [48] and shown in Fig. 2(c). (d)–(f) show the same quantities but calculated in a higher magnetic field of 15.7 T. The dashed red lines show the shift of the incommensurate minimum, from $Q_L \simeq 1.26$ to $Q_L \simeq 1.32$, with increasing magnetic field.

(i.e., with no tetramerization) and spin components along the **a**, **b**, and **c** axes, labeled S_{aa}, S_{bb}, and S_{cc}, respectively. They confirm that modes 1 and 2 are mainly polarized along the **c** and **b** axis, respectively, while modes 3 and 4 are polarized in the three directions **a**, **b**, and **c**. Overall, the mixing of polarization increases with the energy for all excitations.

Note that the total spectral weight of the well-defined excitations is mostly transverse, i.e., polarized perpendicular to **a**. Longitudinal spin dynamics (polarized along **a**) is hardly observed in this 12-T magnetic phase at low energy, in contrast to the zero-field phase [30]. On the other hand, a continuum of excitations is clearly visible at 12 T in the longitudinal channel with a minimum at ≈2 meV.

C. Identification of the collective modes

It is quite difficult to single out the excitation modes in the above results. This is due to the fact that the crystalline structure of $BaCo_2V_2O_8$ induces a significant complication on the spin excitation spectrum. In particular, it is necessary to include four ions in the unit cell (along **c**) to get a proper description of a single chain. This redundancy, with respect to an ideal uniform chain where spins would be placed regularly along the chain, gives rise to folding effects, and more specifically to four replicas of the main dispersions, shifted along the $\mathbf{c}^*$ direction by one reciprocal lattice unit ($\Delta Q_L = 1$).

To illustrate this point, it is useful to consider the simplified model given by Eq. (4), where the spins occupy the sites of such a simple linear spin chain. Figures 5(a)–5(c) show the calculated dynamical structure factors S_{aa}, S_{bb}, and S_{cc} for the $\tilde{g}$ tensor values $(g_{ba}, g_{bb}) = (0.94, 2.35)$, which correspond to $BaCo_2V_2O_8$. The spectrum includes a continuum along with dispersing modes, and a one-to-one correspondence can be easily done with the full results displayed in Figs. 2(a) and 2(d). Mode 1 is visible in S_{cc} [Fig. 5(c)], while mode 2 is visible in S_{bb} [Fig. 5(b)]. The continuum as well as the dispersions of the modes have been reproduced in Fig. 6(a), using reduced wave vectors expressed both in terms of the actual reciprocal units $2\pi/c$ (upper scale) and in terms of $1/c_0$ (lower scale). The minimum of the continuum occurs at the "antiferromagnetic point" $Q = \pi/c_0$, which translates into the reduced value $2 \times \frac{2\pi}{c}$ for the actual screw chains of $BaCo_2V_2O_8$. Similar correspondences can be done for the dispersive features. Interestingly, the latter shall be described over a period consisting of 4 r.l.u.

Figure 6(b) shows a sketch of the full spectrum, including the replicas, to be compared with the actual case of $BaCo_2V_2O_8$. The portion of reciprocal space probed in Fig. 2 is highlighted by an orange rectangle.

This analysis shows that the lowest interlaced energy modes, modes 1 and 2, are thus basically identical. A noticeable difference between the experimental and calculated maps is the size of the gaps, which is different in the measurements at $Q_L = 1$ and $Q_L = 2$. This indicates a dispersion along the **a** and **b** directions resulting from the interchain coupling that is not fully captured by the mean-field treatment in the calculations. Interestingly, two higher-energy modes, modes 3 and 4, are also visible although less clearly, which also seem to be basically identical.

The spectral weight of the different modes also varies at various "equivalent" Q_L positions. This is related not only to an interference effect due to the atomic positions but also to the fact that neutrons are sensitive only to the magnetic correlations between spin components perpendicular to the

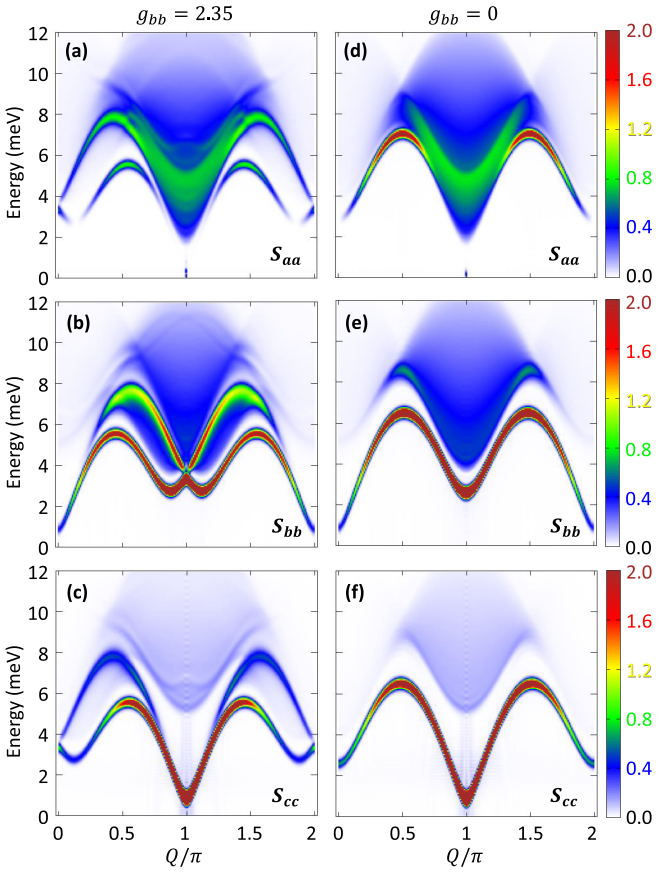

FIG. 5. Dynamical susceptibility calculated for the simplified model of Eq. (4) describing a linear spin chain with $\epsilon = 0.53$, $\mu_0 H = 12$ T. (g_{ba}, g_{bb}) are equal to (0.94,2.35) for (a)–(c) and equal to (0.94,0) for (d)–(f). The components of dynamical susceptibility (a) and (d) S_{aa}, (b) and (e) S_{bb}, and (c) and (f) S_{cc} are shown. In contrast to all other theoretical results, the squared neutron magnetic form factor $f^2(Q)$ of Co^{2+} was not included in these calculations, which are not directly compared with experiments.

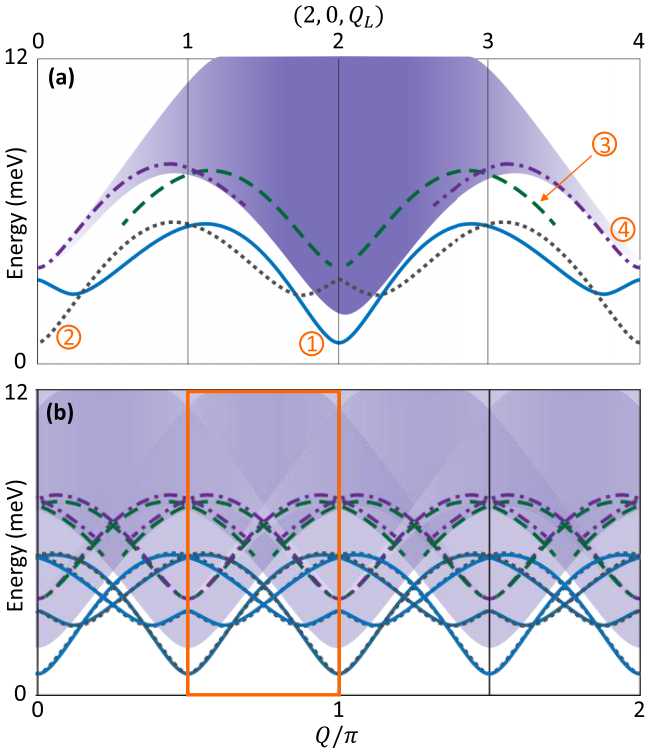

FIG. 6. Schematic drawing of the excitation spectrum of $BaCo_2V_2O_8$ with the same labeling of the modes as in Fig. 2 without (a) and with (b) the replica due to the presence of four ions in the lattice unit cell describing the screw chains (see Sec. III C).

scattering vector. This explains the difference in both maps of Figs. 2(a) and 2(d), with, in particular, the absence of mode 1 in the $(0, 0, Q_L)$ map since, as discussed above, it is mainly polarized along the **c** direction.

D. Shape of the dispersions

It is worth noting that modes 1 and 2 present two kinds of minima, located at commensurate and incommensurate positions. As shown in Fig. 2 and schematized in Fig. 6, they are located at $Q_L = 2$ (modulo 1) and at $Q_L \simeq 1.74$ and $Q_L \simeq 2.26$ (modulo 1), respectively.

Although the effect of the uniform magnetic field is relatively minor compared with the effect of the staggered one, it is nevertheless responsible for this incommensurate feature. To prove this relationship, we performed numerical calculations using the simplified linear spin-chain model equation (4). Figures 5(d)–5(f) show the calculations carried out for $(g_{ba}, g_{bb}) = (0.94, 0)$, i.e., without uniform field. The comparison with Figs. 5(b) and 5(e) demonstrates that the incommensurate features in the spectrum only appear in the presence of the external uniform magnetic field. In addition, as shown in Figs. 5(b) and 5(e) as well as Figs. 5(c) and 5(f), it is clear that the uniform field produces the minima at incommensurate positions around $Q/\pi = 0$ for S_{aa} and around $Q/\pi = 1$ for S_{bb}. In Appendix B, we also show how this incommensurability can be understood from the viewpoint of the bosonized field theory [7].

Furthermore, the incommensurability shifts from π to 0 in reduced momentum transfer with increasing magnetic field, as already mentioned by Matsuda *et al.* [22]. In this spirit, numerical calculations were also performed at a higher magnetic field of 15.7 T, as shown in Figs. 4(d)–4(f). With increasing field, the energy gaps increase not only at the minimum of the dispersion but also at the incommensurate positions, so that the whole excitation spectrum is pushed upward in energy. The incommensurate minimum of modes 1 and 2 is also shifted with the field by approximately 0.06 r.l.u. [see red dashed lines in Figs. 4(b) and 4(e)]. The increase in the shift from the wave number $Q_L =$ integer with increasing field can also be understood in the bosonized field theory since the $\nabla\phi(x)$ term (see Appendix B) becomes larger due to the increase of the uniform field along the **b** axis.

IV. DISCUSSION

$BaCo_2V_2O_8$ is a model system of the XXZ spin-chain antiferromagnet. In zero field, its easy-axis anisotropy along the **c** axis forces the magnetic moments to lie along the **c** axis in a Néel order driven by the interchain coupling. This is opposed

by effective staggered and uniform magnetic field along the **a** and **b** axes, respectively, both produced by the combination of a uniform magnetic field applied along **b** and of the nondiagonal g tensor. This competition between the antiferromagnetic orders along the **a** and **c** directions provokes a quantum phase transition at 10 T. This transition is in the universality class of the transverse field Ising model [19] as identified from the dual-field double-sine Gordon model [23,40]. However, it is important to note that the dispersion of excitations in the two phases surrounding the transition is quite different from that of a transverse field Ising model. Indeed, in the low-field phase, the terms proportional to ϵ in the Hamiltonian lead to the dynamics of domain walls (spinons) even at zero magnetic field, i.e., the excitations have a momentum-dependent dispersion different from the transverse field Ising model (see Appendix A).

As emphasized in our previous works [23,40], the spinons correspond to solitons of the ϕ bosonic field [7] in the language of the bosonized field theory. They are confined by the weak effective potential induced from the interchain interaction. In contrast, in the high-field phase, the new excitations are solitons of the θ bosonic field, which is conjugate to ϕ. The transition at $\mu_0 H_c$ was thus characterized as a topological transition from the ϕ-locked phase to the θ-locked one. More precisely, the excitations come into strongly bounded pairs of θ solitons, sitting on neighboring sites and confined by the large staggered field in the **a** direction arising from the nondiagonal g tensor. Modes 1 and 2 discussed above are constructed on the basis of these pairs of θ solitons: As sketched in Fig. 1(c), the hopping is actually accompanied by a flip from the $S_a = \pm 1$ to the $S_a = \mp 1$ index. As a result, modes 1 and 2 are linear combinations of those solitons, forming transverse excitations with respect to the **a** axis and polarized along the **b** or **c** axis. It is worth noticing that, beyond these well-defined modes, some continuum is still visible in the S_{bb} and S_{aa} components, hence pointing to the persistence of deconfined excitations which remain longitudinal to some extent.

It is thus also clear from this physical analysis that the interchain interactions become less relevant above $\mu_0 H_c$. At low field, the series of discrete energies is a direct manifestation of the linear potential between ϕ solitons induced by those interchain couplings. Each mode corresponds to a typical average distance between solitons. In contrast, in the high-field phase, the interchain interactions play little role: Not only is the magnetic structure dictated by the staggered field, but also this field confines the θ solitons into bound pairs separated by one site [see Fig. 1(c)]. As a result, the concept of typical distance between solitons disappears above $\mu_0 H_c$. It remains that the interchain couplings likely need additional analysis: A more rigorous treatment beyond the mean-field approximation may bring some new insight. In the same spirit, a more detailed description involving different exchange paths along with anisotropic versus isotropic coupling constants could be interesting to investigate in future work.

We also comment on the four-site periodic perturbation which causes the anticrossing of dispersion studied in Sec. III A. Although we show that the tetramerization can explain the anticrossing, such a perturbation would also stabilize a magnetization plateau at half of the saturation value of magnetization. This behavior is different from the measured magnetization curve [13], whose derivative with respect to the field shows a peak-shaped anomaly at half of the saturation magnetization. Another possible route to get a term with four-site periodicity and which would be more consistent with the magnetization curve could be to consider another kind of perturbation: a Dzyaloshinskii-Moriya (DM) interaction with the DM vector spiraling in the *ab* plane with the four-site period. Such a perturbation is compatible with the geometry of the material and would have an effect on the magnetization consistent with the observations. However, this spiral DM interaction does not fully explain the shape of the dispersion in the neutron spectrum, as shown by additional numerical calculations. Possible other origins of the four-site periodicity could be found in the complicated interchain effects arising from the spiral structure of $BaCo_2V_2O_8$. The explanation of the observed anticrossing remains an interesting open question which definitely deserves further investigation. It goes, however, beyond the scope of this paper.

V. CONCLUSION

$BaCo_2V_2O_8$ is a very rich material gathering, from its chemical and crystallographic architecture, many ingredients at the origin of remarkable behaviors in the field of quantum magnetism: Ising-like anisotropy, large intrachain versus weak but non-negligible interchain interactions, an anisotropic g tensor producing easy-axis anisotropy, and effective staggered fields under the application of an external magnetic field. Our combined experimental and numerical study of the full dispersive spectrum along the chain direction allows us to understand and pinpoint the role of each parameter, in particular, of both uniform and staggered fields, in the spin dynamics when considering the problem of a magnetic field applied perpendicular to the chain axis. It also provides an understanding of the properties of solitonic excitations, well beyond the canonical spinon continuum of the isotropic Heisenberg chain of spin 1/2.

ACKNOWLEDGMENTS

We thank E. Villard and B. Vettard for their technical support during the inelastic neutron scattering measurements on ThALES and IN12, respectively, and J. Debray, A. Hadj-Azzem, and J. Balay for their contributions to the crystal growth, cut, and orientation. We acknowledge ILL for allocation of neutron beamtime. S.T. is supported by JSPS KAKENHI Grant No. JP21K03412 and JST CREST Grant No. JPMJCR19T3, Japan. This work was supported in part by the Swiss National Science Foundation under Division II. We also acknowledge financial support from the Fédération Française de Diffusion Neutronique (2FDN).

APPENDIX A: EXCITATIONS AND COMPARISON WITH THE TRANSVERSE FIELD ISING MODEL

As discussed already in Ref. [23], the main features of $BaCo_2V_2O_8$ are described by the Hamiltonian equation (1). Although this Hamiltonian itself is quite complicated, three main features are clearly important for describing its basic

physics: (i) the large Ising anisotropy along the **c** direction; (ii) the staggered transverse magnetic field along the **a** axis, which is created by the staggered g tensor and by the presence of the uniform magnetic field applied along the **b** axis; and (iii) the weak interchain coupling.

In order to analyze the physics of the system, it is convenient to first discuss the simplified Hamiltonian given by Eq. (4). In the first step, both the interchain coupling and the uniform magnetic field are ignored to focus on the effects of the staggered transverse field. This leads to the strictly one-dimensional Hamiltonian

$$\mathcal{H}_{\text{stag}} = J\sum_n \left[\epsilon\left(S_n^a S_{n+1}^a + S_n^b S_{n+1}^b\right) + S_n^c S_{n+1}^c\right] - \tilde{h}_a \sum_n (-1)^n S_n^a, \tag{A1}$$

where c corresponds to the Ising axis and $\tilde{h}_a$ is the staggered part of the magnetic field, in which the g and μ_{B} factors have been absorbed.

An even simpler version of this Hamiltonian would be to completely neglect the ϵ term leading to a purely Ising Hamiltonian along the chains:

$$\mathcal{H}_{\text{Ising}} = J\sum_n S_n^c S_{n+1}^c - \tilde{h}_a \sum_n (-1)^n S_n^a. \tag{A2}$$

For this Hamiltonian, a simple gauge transformation $\tilde{S}_n^{a,b} = (-1)^n S_n^{a,b}$, $\tilde{S}_n^c = S_n^c$ removes the oscillating term and brings the problem back to the standard form of the transverse field Ising model:

$$\mathcal{H}_{\text{trans}} = J\sum_n \tilde{S}_n^c \tilde{S}_{n+1}^c - \tilde{h}_a \sum_n \tilde{S}_n^a. \tag{A3}$$

This Hamiltonian, which can be fully solved by a mapping onto free fermions [19], has a celebrated quantum phase transition separating two phases, one dominated by a staggered order along the c direction and one with a uniform polarization of the $\tilde{S}_n^a$ operator (and thus a staggered order for S_n^a).

One might thus naively think that the physics of (A1) is simply that of the transverse field Ising model up to the gauge transformation. This naive view, however, is not correct, and although the quantum phase transition occurring in (A1) is indeed in the universality class of the Ising model [23,40], the nature of the phases, in particular, the dispersion of the excitations, is strongly affected by the $S_n^a S_{n+1}^a$ and $S_n^b S_{n+1}^b$ terms present in Eq. (A1) and absent in Eq. (A2). For example, in the absence of a magnetic field, Eq. (A1) has a dispersion of the excitation due to the term $S_n^a S_{n+1}^a + S_n^b S_{n+1}^b = \frac{1}{2}(S_n^+ S_{n+1}^- + S_n^- S_{n+1}^+)$, while an excitation created in the chain described by Eq. (A2) is unable to move. Such a difference between the models is of course crucial when comparing with the neutron scattering spectra, which clearly demonstrates the strongly dispersing nature of the excitations.

To illustrate this point, let us first carry out the gauge transformation to bring the staggered field into a uniform one, leading to

$$\mathcal{H}_{\text{stag}} = J\sum_n \left[-\epsilon\left(\tilde{S}_n^a \tilde{S}_{n+1}^a + \tilde{S}_n^b \tilde{S}_{n+1}^b\right) + S_n^c S_{n+1}^c\right] - \tilde{h}_a \sum_n \tilde{S}_n^a. \tag{A4}$$

We then can use the Kramers-Wannier transformation [50]

$$\tau_{n+\frac{1}{2}}^b = \prod_{p=1}^n \sigma_p^a, \quad \tau_{n+\frac{1}{2}}^c = \sigma_n^c \sigma_{n+1}^c, \tag{A5}$$

to rewrite the Hamiltonian in terms of the bond operators, where σ_n^α and τ_n^α are Pauli matrices, and $S_n^\alpha = \frac{1}{2}\sigma_n^\alpha$. Then the Hamiltonian is transformed into

$$\mathcal{H}_{\text{stag}} = \frac{J}{4}\sum_n \left[\epsilon\left(-1+\tau_{n+\frac{1}{2}}^c\right)\tau_{n-\frac{1}{2}}^b \tau_{n+\frac{3}{2}}^b + \tau_{n+\frac{1}{2}}^c\right] - \frac{\tilde{h}_a}{2}\sum_n \tau_{n-\frac{1}{2}}^b \tau_{n+\frac{1}{2}}^b. \tag{A6}$$

In this representation, the Néel order along the c axis existing in the original chain for $\tilde{h}_a = 0$ corresponds to the uniform polarization along the $\tau^c = -1$ direction in the τ representation. The excitations, which are the spinons of the original model, correspond to simply flipping a single spin in the latter. When $\epsilon = \tilde{h}_a = 0$, such excitations would have no dynamics, as is the case of the transverse field Ising model. Such dynamics only appears in the transverse field Ising model when $\tilde{h}_a$ is nonzero. As can be seen from Eq. (A6), the $\tilde{h}_a$ term causes a hopping between two nearest neighbors and thus allows the spinon to hop by *one* lattice site. This gives rise to terms dispersing as $\cos(ka)$ in the excitation spectrum.

In contrast, the ϵ term in the XXZ model leads to a quite different dispersion. Indeed, *even* at $\tilde{h}_a = 0$, such terms allow the spinons to move. In Eq. (A6) for $\tilde{h}_a = 0$, $\epsilon(-1+\tau_{n+\frac{1}{2}}^c) \simeq \epsilon(-1+\langle\tau_{n+\frac{1}{2}}^c\rangle) \neq 0$, and the $\tau_{n-\frac{1}{2}}^b \tau_{n+\frac{3}{2}}^b$ term connects the sites $n-\frac{1}{2}$ and $n+\frac{3}{2}$, which allows the spinon to move by *two* lattice spacings, as can also be directly seen by other methods [7]. As a result, the modes have a dispersion which is essentially $\cos(2ka)$. The excitations in the low-field phase thus have a different structure and a different dispersion relation than the ones predicted by the transverse field Ising model.

In the high-transverse-field phase, the uniform field in Eq. (A4) is dominant in the Hamiltonian, and the magnetic order in the $+\tilde{S}_n^a$ direction grows. In this sense, the situation is similar to the disordered phase of the transverse field Ising model. However, the uniform field along the b axis, which is neglected in Eq. (A1) for simplicity, affects the dispersion, as we discussed in the main text.

Another illustration of this physics is provided by the field theory representation of the Hamiltonian equation (A1) established in Ref. [23]. The field theoretical approach for the high-field phase is discussed in Appendix B.

APPENDIX B: BOSONIZED FIELD THEORY

We consider the simplified model equation (4) with retaking the spin axes as $S_n^a \to S_n^a$, $S_n^b \to S_n^c$, and $S_n^c \to -S_n^b$ ($\pi/2$ rotation around the a axis),

$$\mathcal{H} = J\sum_n \left(\epsilon S_n^a S_{n+1}^a + S_n^b S_{n+1}^b + \epsilon S_n^c S_{n+1}^c\right) - g_{ba}\mu_{\text{B}}\mu_0 H\sum_n (-1)^n S_n^a - g_{bb}\mu_{\text{B}}\mu_0 H\sum_n S_n^c$$

$$= J \sum_n \frac{1+\epsilon}{2}\Big[\big(S^a_n S^a_{n+1} + S^b_n S^b_{n+1}\big) + \frac{2\epsilon}{1+\epsilon} S^c_n S^c_{n+1} - \frac{1-\epsilon}{1+\epsilon}\big(S^a_n S^a_{n+1} - S^b_n S^b_{n+1}\big)\Big] - g_{ba}\mu_B\mu_0 H \sum_n (-1)^n S^a_n - g_{bb}\mu_B\mu_0 H \sum_n S^c_n. \quad \text{(B1)}$$

The bosonization formulas for the spin operators are [7]

$$S^c_j \simeq -\frac{c_0}{\pi}\frac{d\phi(z)}{dz} + a_1(-1)^j \cos[2\phi(z)],$$
$$S^+_j \simeq e^{-i\theta(z)}\{b_0(-1)^j + b_1 \cos[2\phi(z)]\}, \quad \text{(B2)}$$

where c_0 is the lattice constant and a_1, b_0, and b_1 are some constants. Conjugate bosonic fields 2ϕ and θ can intuitively be considered as the polar and azimuthal angles of the Néel order. The terms appearing in the Hamiltonian are bosonized following [7,40]

$$\sum_n \big(S^a_n S^a_{n+1} - S^b_n S^b_{n+1}\big) \simeq -\int dz \cos[2\theta(z)],$$
$$\sum_n S^c_n \simeq -\frac{1}{\pi}\int dz \nabla\phi(z),$$
$$\sum_n (-1)^n S^a_n \simeq \int dz \cos\theta(z).$$

Thus the bosonized field theory is given as

$$\mathcal{H}_{\text{bos}} = \frac{1}{2\pi}\int dz\Big[uK(\nabla\theta)^2 + \frac{u}{K}(\nabla\phi)^2\Big] - g_1\int dz \cos[\theta(z)] + g_2\int dz \cos[2\theta(z)] + g_3\int dz \cos[4\phi(z)] + g_4\int dz \nabla\phi(z), \quad \text{(B3)}$$

where u is the spinon velocity and K is the Tomonaga-Luttinger parameter. The g_i are related to the original parameters in (B1): $g_1 \propto H$, $g_2 \propto \frac{J(1-\epsilon)}{1+\epsilon}$, $g_3 \propto \frac{2\epsilon J}{1+\epsilon}$, and $g_4 \propto H$. Since $2\epsilon/(1+\epsilon) < 1$, the $\cos[4\phi(z)]$ term is irrelevant. The $\cos[\theta(z)]$ term is more relevant than the $\cos[2\theta(z)]$ term. Therefore the field $\theta(z)$ is locked at $2n\pi$ (n is an integer). From Eq. (B2), the spin-spin correlation function $\langle S^c_n(t) S^c_0(0)\rangle$ is related to the correlation function of the $\phi(z)$ field. Due to the existence of the $\nabla\phi(z)$ term in Eq. (B3), the dispersion of $S_{cc}(q, \omega)$ excitations has an energy local minimum at some incommensurate momentum.

For the magic value $K = 1/4$ this Hamiltonian can be refermionized [7] and mapped onto a free-fermion model with

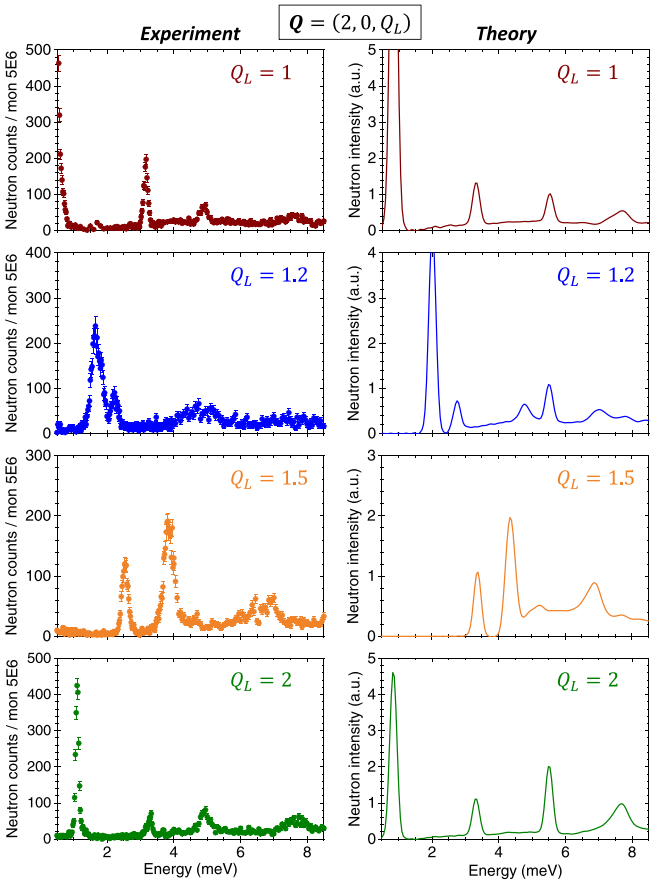

FIG. 7. Constant-**Q** scans at chosen $(2, 0, Q_L)$ values as a function of the energy: those measured on ThALES (left panels) and the calculated ones [48] (right panels). Note that the same scaling ratio is used in all panels between experiment and theory.

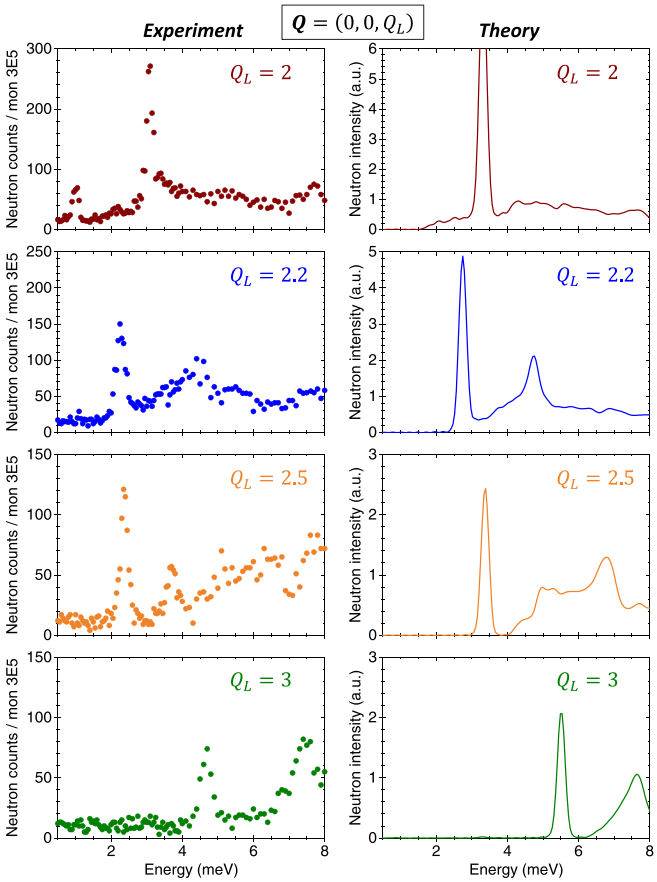

FIG. 8. Constant-**Q** scans at chosen $(0, 0, Q_L)$ values as a function of the energy: those measured on IN12 (left panels) and the calculated ones [48] (right panels). Note that the same scaling ratio is used in all panels between experiment and theory.

both a staggered periodic potential (proportional to g_3) and a pairing term (proportional to g_1). Retaining only these two terms and diagonalizing the fermionic Hamiltonian by the usual Bogoliubov transformation leads for the energy of the lowest mode to

$$E_k = -\sqrt{\xi(k)^2 + (g_3 - g_1)^2}, \tag{B4}$$

with $\xi(k) = -J\epsilon\cos(k)$ and assuming $g_3 > 0$ and $g_1 > 0$. The momentum k is varying between $[0, \pi/2]$. For $g_1 = 0$ one recovers the gap due to the Ising anisotropy. Expanding the square root gives back the spinon dispersion $\cos(2k)$. At the critical point $g_3 = g_1$ the spectrum becomes massless, and the duality of the model is apparent between $g_3 > g_1$ and $g_3 < g_1$ but with an order for the pseudofermions going from an order in the density $g_3 < g_1$ to a pairing order $g_3 < g_1$.

APPENDIX C: NEUTRON ENERGY SCANS COMPARED WITH CALCULATIONS

In order to further compare the experimental and the calculated spectra, constant-**Q** energy scans along $(2, 0, Q_L)$ and $(0, 0, Q_L)$ have been plotted in Figs. 7 and 8. All the experimental features are rather well reproduced by the calculations, although there are some discrepancies concerning the exact energy positions and amplitudes of some peaks. The spurions are also visible at 1 and 8 meV on the experimental energy scans at $(0, 0, 2)$ and $(0, 0, 2.5)$. Some of the discrepancies, in particular, of the low-energy peaks, are due to the mean-field treatment of the interchain coupling.

[1] T. Giamarchi, C. Rüegg, and O. Tchernyshyov, Bose–Einstein condensation in magnetic insulators, Nat. Phys. **4**, 198 (2008).

[2] V. Zapf, M. Jaime, and C. D. Batista, Bose-Einstein condensation in quantum magnets, Rev. Mod. Phys. **86**, 563 (2014).

[3] L. Savary and L. Balents, Quantum spin liquids: A review, Rep. Prog. Phys. **80**, 016502 (2016).

[4] H. Takagi, T. Takayama, G. Jackeli, G. Khaliullin, and S. E. Nagler, Concept and realization of Kitaev quantum spin liquids, Nat. Rev. Phys. **1**, 264 (2019).

[5] J. Alicea, New directions in the pursuit of Majorana fermions in solid state systems, Rep. Prog. Phys. **75**, 076501 (2012).

[6] C. Nisoli, R. Moessner, and P. Schiffer, Colloquium: Artificial spin ice: Designing and imaging magnetic frustration, Rev. Mod. Phys. **85**, 1473 (2013).

[7] T. Giamarchi, *Quantum Physics in One Dimension*, International Series of Monographs on Physics (Clarendon Press, Oxford, 2003), Vol. 121.

[8] B. Lake, D. A. Tennant, C. D. Frost, and S. E. Nagler, Quantum criticality and universal scaling of a quantum antiferromagnet, Nat. Mater. **4**, 329 (2005).

[9] M. Mourigal, M. Enderle, A. Klöpperpieper, J.-S. Caux, A. Stunault, and H. M. Rønnow, Fractional spinon excitations in the quantum Heisenberg antiferromagnetic chain, Nat. Phys. **9**, 435 (2013).

[10] B. Thielemann, C. Rüegg, H. M. Rønnow, A. M. Läuchli, J.-S. Caux, B. Normand, D. Biner, K. W. Krämer, H.-U. Güdel, J. Stahn, K. Habicht, K. Kiefer, M. Boehm, D. F. McMorrow, and J. Mesot, Direct Observation of Magnon Fractionalization in the Quantum Spin Ladder, Phys. Rev. Lett. **102**, 107204 (2009).

[11] S. Ward, P. Bouillot, H. Ryll, K. Kiefer, K. W. Krämer, C. Rüegg, C. Kollath, and T. Giamarchi, Spin ladders and quantum simulators for Tomonaga-Luttinger liquids, J. Phys.: Condens. Matter **25**, 014004 (2012).

[12] V. L. Pokrovsky and A. L. Talapov, Ground State, Spectrum, and Phase Diagram of Two-Dimensional Incommensurate Crystals, Phys. Rev. Lett. **42**, 65 (1979).

[13] S. Kimura, H. Yashiro, K. Okunishi, M. Hagiwara, Z. He, K. Kindo, T. Taniyama, and M. Itoh, Field-Induced Order-Disorder Transition in Antiferromagnetic $BaCo_2V_2O_8$ Driven by a Softening of Spinon Excitation, Phys. Rev. Lett. **99**, 087602 (2007).

[14] S. Kimura, M. Matsuda, T. Masuda, S. Hondo, K. Kaneko, N. Metoki, M. Hagiwara, T. Takeuchi, K. Okunishi, Z. He, K. Kindo, T. Taniyama, and M. Itoh, Longitudinal Spin Density Wave Order in a Quasi-1D Ising-like Quantum Antiferromagnet, Phys. Rev. Lett. **101**, 207201 (2008).

[15] E. Canévet, B. Grenier, M. Klanjšek, C. Berthier, M. Horvatić, V. Simonet, and P. Lejay, Field-induced magnetic behavior in quasi-one-dimensional Ising-like antiferromagnet $BaCo_2V_2O_8$: A single-crystal neutron diffraction study, Phys. Rev. B **87**, 054408 (2013).

[16] Q. Faure, S. Takayoshi, V. Simonet, B. Grenier, M. Månsson, J. S. White, G. S. Tucker, C. Rüegg, P. Lejay, T. Giamarchi, and S. Petit, Tomonaga-Luttinger Liquid Spin Dynamics in the Quasi-One-Dimensional Ising-like Antiferromagnet $BaCo_2V_2O_8$, Phys. Rev. Lett. **123**, 027204 (2019).

[17] Z. Wang, J. Wu, W. Yang, A. K. Bera, D. Kamenskyi, A. N. Islam, S. Xu, J. M. Law, B. Lake, C. Wu, and A. Loidl, Experimental observation of Bethe strings, Nature (London) **554**, 219 (2018).

[18] A. K. Bera, J. Wu, W. Yang, R. Bewley, M. Boehm, J. Xu, M. Bartkowiak, O. Prokhnenko, B. Klemke, A. N. Islam, J. M. Law, Z. Wang, and B. Lake, Dispersions of many-body Bethe strings, Nat. Phys. **16**, 625 (2020).

[19] P. Pfeuty, The one-dimensional Ising model with a transverse field, Ann. Phys. (Amsterdam) **57**, 79 (1970).

[20] R. Coldea, D. Tennant, E. Wheeler, E. Wawrzynska, D. Prabhakaran, M. Telling, K. Habicht, P. Smeibidl, and K. Kiefer, Quantum criticality in an Ising chain: Experimental evidence for emergent E_8 symmetry, Science **327**, 177 (2010).

[21] N. J. Robinson, F. H. L. Essler, I. Cabrera, and R. Coldea, Quasiparticle breakdown in the quasi-one-dimensional Ising ferromagnet $CoNb_2O_6$, Phys. Rev. B **90**, 174406 (2014).

[22] M. Matsuda, H. Onishi, A. Okutani, J. Ma, H. Agrawal, T. Hong, D. M. Pajerowski, J. R. D. Copley, K. Okunishi, M. Mori, S. Kimura, and M. Hagiwara, Magnetic structure and dispersion relation of the $S = \frac{1}{2}$ quasi-one-dimensional Ising-like antiferromagnet $BaCo_2V_2O_8$ in a transverse magnetic field, Phys. Rev. B **96**, 024439 (2017).

[23] Q. Faure, S. Takayoshi, S. Petit, V. Simonet, S. Raymond, L.-P. Regnault, M. Boehm, J. S. White, M. Månsson, C. Rüegg, P.

Lejay, B. Canals, T. Lorenz, S. C. Furuya, T. Giamarchi, and B. Grenier, Topological quantum phase transition in the Ising-like antiferromagnetic spin chain $BaCo_2V_2O_8$, Nat. Phys. **14**, 716 (2018).

[24] Z. Wang, T. Lorenz, D. I. Gorbunov, P. T. Cong, Y. Kohama, S. Niesen, O. Breunig, J. Engelmayer, A. Herman, J. Wu, K. Kindo, J. Wosnitza, S. Zherlitsyn, and A. Loidl, Quantum Criticality of an Ising-like Spin-1/2 Antiferromagnetic Chain in a Transverse Magnetic Field, Phys. Rev. Lett. **120**, 207205 (2018).

[25] Z. Wang, J. Wu, S. Xu, W. Yang, C. Wu, A. K. Bera, A. T. M. N. Islam, B. Lake, D. Kamenskyi, P. Gogoi, H. Engelkamp, N. Wang, J. Deisenhofer, and A. Loidl, From confined spinons to emergent fermions: Observation of elementary magnetic excitations in a transverse-field Ising chain, Phys. Rev. B **94**, 125130 (2016).

[26] Y. Cui, H. Zou, N. Xi, Z. He, Y. X. Yang, L. Shu, G. H. Zhang, Z. Hu, T. Chen, R. Yu, J. Wu, and W. Yu, Quantum Criticality of the Ising-like Screw Chain Antiferromagnet $SrCo_2V_2O_8$ in a Transverse Magnetic Field, Phys. Rev. Lett. **123**, 067203 (2019).

[27] K. Amelin, J. Engelmayer, J. Viirok, U. Nagel, T. Rõõm, T. Lorenz, and Z. Wang, Experimental observation of quantum many-body excitations of E_8 symmetry in the Ising chain ferromagnet $CoNb_2O_6$, Phys. Rev. B **102**, 104431 (2020).

[28] S. Kimura, K. Okunishi, M. Hagiwara, K. Kindo, Z. He, T. Taniyama, M. Itoh, K. Koyama, and K. Watanabe, Collapse of magnetic order of the quasi one-dimensional ising-like antiferromagnet $BaCo_2V_2O_8$ in transverse fields, J. Phys. Soc. Jpn. **82**, 033706 (2013).

[29] Z. He, D. Fu, T. Kyômen, T. Taniyama, and M. Itoh, Crystal growth and magnetic properties of $BaCo_2V_2O_8$, Chem. Mater. **17**, 2924 (2005).

[30] B. Grenier, S. Petit, V. Simonet, E. Canévet, L.-P. Regnault, S. Raymond, B. Canals, C. Berthier, and P. Lejay, Longitudinal and Transverse Zeeman Ladders in the Ising-like Chain Antiferromagnet $BaCo_2V_2O_8$, Phys. Rev. Lett. **114**, 017201 (2015).

[31] A. K. Bera, B. Lake, W.-D. Stein, and S. Zander, Magnetic correlations of the quasi-one-dimensional half-integer spin-chain antiferromagnets $SrM_2V_2O_8$ (M = Co, Mn), Phys. Rev. B **89**, 094402 (2014).

[32] A. K. Bera, B. Lake, F. H. L. Essler, L. Vanderstraeten, C. Hubig, U. Schollwöck, A. T. M. N. Islam, A. Schneidewind, and D. L. Quintero-Castro, Spinon confinement in a quasi-one-dimensional anisotropic Heisenberg magnet, Phys. Rev. B **96**, 054423 (2017).

[33] N. Ishimura and H. Shiba, Dynamical correlation functions of one-dimensional anisotropic Heisenberg model with spin 1/2. I: Ising-like antiferromagnets, Prog. Theor. Phys. **63**, 743 (1980).

[34] M. Kenzelmann, Y. Chen, C. Broholm, D. H. Reich, and Y. Qiu, Bound Spinons in an Antiferromagnetic S = 1/2 Chain with a Staggered Field, Phys. Rev. Lett. **93**, 017204 (2004).

[35] Z. Wang, M. Schmidt, A. K. Bera, A. T. M. N. Islam, B. Lake, A. Loidl, and J. Deisenhofer, Spinon confinement in the one-dimensional Ising-like antiferromagnet $SrCo_2V_2O_8$, Phys. Rev. B **91**, 140404(R) (2015).

[36] M. Oshikawa and I. Affleck, Field-Induced Gap in S = 1/2 Antiferromagnetic Chains, Phys. Rev. Lett. **79**, 2883 (1997).

[37] I. Affleck and M. Oshikawa, Field-induced gap in Cu benzoate and other S = 1/2 antiferromagnetic chains, Phys. Rev. B **60**, 1038 (1999).

[38] S. B. Rutkevich, Kink confinement in the antiferromagnetic XXZ spin-(1/2) chain in a weak staggered magnetic field, Europhys. Lett. **121**, 37001 (2018).

[39] A. Okutani, S. Kimura, T. Takeuchi, and M. Hagiwara, High-field multi-frequency ESR in the quasi-1D S = 1/2 Ising-like antiferromagnet $BaCo_2V_2O_8$ in a transverse field, Appl. Magn. Reson. **46**, 1003 (2015).

[40] S. Takayoshi, S. C. Furuya, and T. Giamarchi, Topological transition between competing orders in quantum spin chains, Phys. Rev. B **98**, 184429 (2018).

[41] G. Vidal, Classical Simulation of Infinite-Size Quantum Lattice Systems in One Spatial Dimension, Phys. Rev. Lett. **98**, 070201 (2007).

[42] P. Lejay, E. Canevet, S. Srivastava, B. Grenier, M. Klanjsek, and C. Berthier, Crystal growth and magnetic property of $MCo_2V_2O_8$ (M = Sr and Ba), J. Cryst. Growth **317**, 128 (2011).

[43] M. Boehm, P. Steffens, J. Kulda, M. Klicpera, S. Roux, P. Courtois, P. Svoboda, J. Saroun, and V. Sechovsky, ThALES-Three Axis Low Energy Spectroscopy for highly correlated electron systems, Neutron News **26**(3), 18 (2015).

[44] K. Schmalzl, W. Schmidt, S. Raymond, H. Feilbach, C. Mounier, B. Vettard, and T. Brueckel, The upgrade of the cold neutron three-axis spectrometer IN12 at the ILL, Nucl. Instrum. Methods Phys. Res. Sect. A **819**, 89 (2016).

[45] M. Klanjšek, M. Horvatić, S. Krämer, S. Mukhopadhyay, H. Mayaffre, C. Berthier, E. Canévet, B. Grenier, P. Lejay, and E. Orignac, Giant magnetic field dependence of the coupling between spin chains in $BaCo_2V_2O_8$, Phys. Rev. B **92**, 060408(R) (2015).

[46] I. P. McCulloch, Infinite size density matrix renormalization group, revisited, arXiv:0804.2509.

[47] H. N. Phien, G. Vidal, and I. P. McCulloch, Infinite boundary conditions for matrix product state calculations, Phys. Rev. B **86**, 245107 (2012).

[48] The neutron magnetic form factor $f(q)$, included as $f^2(q)$ in the calculated data to match the experiments, is calculated from the analytical expression of the $\langle j_0 \rangle$ form factor for Co^{2+} using the tabulated coefficients from P. J. Brown, Magnetic form factors, in *International Tables of Crystallography, Volume C: Mathematical Physical and Chemical Tables*, edited by A. J. C. Wilson (International Union of Crystallography, Kluwer, London, 1996), Sec. 4.4.5, pp. 454–461.

[49] S. K. Niesen, G. Kolland, M. Seher, O. Breunig, M. Valldor, M. Braden, B. Grenier, and T. Lorenz, Magnetic phase diagrams, domain switching, and quantum phase transition of the quasi-one-dimensional Ising-like antiferromagnet $BaCo_2V_2O_8$, Phys. Rev. B **87**, 224413 (2013).

[50] H. A. Kramers and G. H. Wannier, Statistics of the two-dimensional ferromagnet. Part I, Phys. Rev. **60**, 252 (1941).